https://doi.org/10.5194/egusphere-2026-1388
Preprint. Discussion started: 27 March 2026

Effect of Design Storm Characterization on Flood Exposure and Structure Damage Estimates: A Case Study in South Louisiana, USA.

Mohamed ElSaadani[1,2], Emad Habib[1,2], Mohamed M. Morsy[3,2]

[1]Department of Civil Engineering, University of Louisiana at Lafayette, Lafayette, 70504, United States
[2]Louisiana Watershed Flood Center, University of Louisiana at Lafayette, Lafayette, 70504, United States
[3]Irrigation and Hydraulics Engineering Department, Faculty of Engineering, Cairo University, P.O. Box 12211, Giza 12613, Egypt

Correspondence to: Emad Habib (habib@louisiana.edu)

Abstract. Quantitative flood risk assessments rely on rainfall frequency analysis to define Annual exceedance probability (AEP) storms, commonly referred to as design storms, for generating flood hazard maps and expected annual damage curves. Current engineering practice typically employs spatially uniform design storms derived from point-based gauge statistics; however, this approach suppresses the spatial organization and intensity gradients present in observed storms. Stochastic storm transposition (SST) offers an alternative by preserving the spatial structure of observed rainfall and stochastically repositioning full storm fields across a watershed. Although recent work shows that SST-based design storms can alter peak discharge estimates relative to uniform storms, their implications for flood inundation mapping and for estimating structural damage and their resulting monetary losses remain understudied. This study addresses that gap by comparing flood exposure and damages produced by both design-storm approaches in the Vermilion River Basin, a low-gradient inland–coastal watershed in south-central Louisiana. The comparison reveals that SST identifies 11,518 buildings inundated in at least one SST realization but missed entirely by Atlas 14, representing over ~$110M in cumulative structural damages. The divergence between the two approaches is concentrated in mid-elevation urban neighborhoods, where spatial rainfall variability activates flooding thresholds that uniform storms cannot trigger. These results demonstrate that uniform design storms systematically underestimate both the catastrophic tail and the breadth of flood exposure in low-gradient basins.

1 Introduction

Quantitative flood-risk assessments rely on the consistent linkage of flood hazard characterization, exposure, and economic loss estimation. Within this chain, rainfall frequency analysis and the derivation of design discharges are central to estimating flood damage risk, as they determine the exceedance probabilities that underpin hazard maps and expected annual damage curves (Merz et al., 2002; Merz et al., 2008; Büchele et al., 2006; Nofal et al., 2022). This study investigates how the choice of annual exceedance probability (AEP) storms, commonly referred to as design storms, affects structure damage estimates in a low-gradient inland-to-coastal (transitional) basin. Typically, direct flood damage is estimated by intersecting inundation maps with representations of the building stock and translating water depths into monetary losses using depth-damage

https://doi.org/10.5194/egusphere-2026-1388
Preprint. Discussion started: 27 March 2026

relationships or more detailed vulnerability models (e.g., Dutta et al., 2003; Scawthorn et al., 2006; Schwarz and Maiwald, 2009). Merz et al. (2010) summarize this workflow as a sequence of (i) exposure analysis, which identifies elements at risk and their asset values, (ii) susceptibility analysis, which describes how these elements respond to flooding, and (iii) aggregation of losses across sectors such as private households, services, industry, public infrastructure, and lifelines. They emphasize that, despite the central role of damage estimates in benefit-cost analysis, risk mapping, and insurance pricing, damage data are sparse, methods are often crude, and model formulations are frequently transferred across regions, time periods, and damage processes without sufficient justification. In this study, we focus on improving the methods used for flood risk mapping and structure damage estimation by evaluating how the usual simplifications in defining design rainfall shape the resulting flood maps and the losses inferred from them.

A wide spectrum of approaches is used to model the flood damage estimation workflow from triggering weather events to flood damage. These range from relatively simple combinations of flood frequency analysis with stage-damage curves (e.g., Merz et al., 2002) to fully distributed hydrologic-hydraulic simulations that resolve inundation dynamics and building-scale exposure (e.g., Dutta et al., 2003; Apel et al., 2004 and 2008). Merz et al. (2008) frame flood risk as the probability of adverse consequences due to inundation and demonstrate with a case study in Germany that the total uncertainty in risk estimates arises from the superposition of multiple components, including flood frequency, rating-curve uncertainty, and depth-damage relationships. Their Monte Carlo analysis shows that damage estimation dominates uncertainty for relatively frequent events, whereas flood frequency estimates dominate for larger return periods, and that ignoring these uncertainties can materially affect mitigation decisions. Pavesi et al. (2024) and Merz et al. (2008) also highlight a practical tension: great detail hydraulic models are often required for credible inundation mapping, but their computational cost discourages the ensemble simulations needed for rigorous uncertainty analysis, especially over large river reaches. Pavesi et al. (2024) emphasized that although simplifying modeling assumptions leads to easy implementations, enduring a higher computational cost by adopting finer modeling detail can lead to improved flood risk maps.

Recent comparative studies show that exposure and damage estimates are highly sensitive not only to the choice of damage model but also to how flooding exposure is estimated. Gutenson et al. (2023) showed that different inundation mapping approaches for Hurricane Harvey produced loss estimates that differed by more than an order of magnitude, with resulting differences exceeding billions of dollars. Grimley et al. (2025) showed that transition-zone dynamics during Hurricane Florence, where inland runoff and coastal surge interact, can elevate water levels beyond what would be obtained from purely coastal or purely upland drivers, implying that partial representations of the physical system may underestimate risk in compound settings. These studies, along with broader work on compound flooding (e.g., Moftakhari et al., 2017), highlight the need for damage assessments coupled with flood models that capture the dominant physical mechanisms, rather than simplified or single-driver configurations.

The challenges in flood risk assessment, therefore, extend beyond damage functions or model parameters to the underlying hazard representation. Bodoque et al. (2023) and Merz et al. (2010) note that flood damage assessment has historically lagged flood hazard analysis and that deterministic scenarios are still commonly used in regulatory and engineering practice. In the

https://doi.org/10.5194/egusphere-2026-1388
Preprint. Discussion started: 27 March 2026

United States, hazard products and design guidance remain anchored to past conditions, using maps such as the United States Federal Emergency Management Agency (FEMA)'s Special Flood Hazard Areas and point-based intensity-duration-frequency curves like NOAA Atlas 14 (Perica et al., 2013). Wing et al. (2022) show that FEMA's current floodplain maps capture only about 41% of contemporary flood risk, implying that many exposed structures are systematically missed. The non-stationarity of extreme precipitation documented by Milly et al. (2008) adds to this problem, because biases in how historical storms are represented translate directly into biased estimates of flood losses.

Conventional practice assumes a one-to-one correspondence between rainfall and discharge return periods, using spatially uniform design storms derived from gauge-based statistics and, where needed, depth-area reduction factors such as those in TP40. Wright et al. (2013, 2014, 2019) and Zhu et al. (2018) show that this assumption can break down, especially in smaller basins where flood response is controlled by the alignment of intense storm cells with watershed structure. Wright et al. (2014) used NCEP Stage IV (Nelson et al., 2016; Eldardiry et al., 2015 and 2017) radar-based stochastic storm transposition (SST) to generate long records of transposed space-time rainfall and demonstrated that uniform, deterministic rainfall-based flood estimates may substantially underestimate peak discharges in some sub-watersheds. This underestimation is particularly evident in small, fast-responding sub-watersheds where flooding is driven by short-duration, highly localized convective storms rather than long-duration basin-wide rainfall. Wright et al. (2014) also showed that the relationship between rainfall and discharge return period depends strongly on basin scale, storm organization, and land-surface properties. SST provides a physically-based alternative to deterministic, spatially uniform storms by treating historically observed storms as space-time rainfall fields and repositioning them within a homogeneous extreme-rainfall domain, preserving internal intensity gradients and temporal evolution while exploring a wide range of plausible storm placements relative to the drainage network. SST, therefore, can substantially improve the rainfall hazard inputs that control inundation depth patterns and, by extension, structure damage estimates.

Spatial rainfall representation can be important in hydrologically complex, low-gradient systems such as the current study area the Vermilion River Basin (VRB) in south-central Louisiana, where inundation is governed by the timing and spatial alignment of tributary peaks, floodplain storage, and backwater effects from coastal boundary conditions (Awaad et al., 2025; Saad and Habib, 2021; Saad et al., 2021). This study investigates how shifts in storm spatial-temporal representation and placement can change knowledge of both where flooding occurs and the depth of flooding, with direct implications for structure damage estimates and mitigation priorities.

This study addresses a gap at the intersection of design storm selection, high-resolution hydraulic modeling, and economic loss estimation. We evaluate building-level flood damage in the VRB under two contrasting hazard definitions of the 100-year, 24-hour event: (1) a deterministic, spatially uniform NOAA Atlas 14 AEP storm, spatially adjusted using Technical Paper 40 (TP40; Hershfield, 1961) depth-area relationships, and (2) an ensemble of fifty SST realizations constructed from gauge-adjusted radar rainfall fields.

We use a calibrated hydrologic-hydrodynamic coupled model developed as part of the Louisiana Watershed Initiative (LWI 2025; Miles et al., 2025; Habib et al., 2025) with a detailed representation of channels, floodplain storage, and hydraulic

https://doi.org/10.5194/egusphere-2026-1388
Preprint. Discussion started: 27 March 2026

structures to simulate flood inundation depths and extents in the VRB low-gradient inland-coastal watershed. The resulting depth fields are intersected with the National Structure Inventory (NSI; Gutenson et al., 2023) and converted to structure economic losses using standardized United States Army Corps of Engineers (USACE) depth-damage functions (Dunn 2000), allowing for assessing how alternative hazard definitions change inundation extent, depth distributions, exposure, and the distribution of basin-wide damages.

The remainder of this paper is organized as follows. Sect, 2 introduces the Vermilion River Basin and its hydrologic setting. Sect, 3 describes the rainfall forcing scenarios, the coupled hydrologic-hydrodynamic modeling framework, and the damage estimation analysis. Sect, 4 examines how the choice of rainfall representation affects the distribution of inundation depth, estimates of aggregate damages and exposure gaps, and the spatial organization of inundation clusters. Sect. 5 discusses what the results imply for flood-risk assessment in our study area. Finally, we summarize our main conclusions in Sect. 6.

2 Study Area

The VRB (Fig. 1) is a low-gradient inland-coastal watershed in south-central Louisiana, USA. The basin drains an area of approximately 1,500 km² into the Vermilion Bay and the Gulf of Mexico. The Vermilion River collects runoff from a dense network of small tributaries that drain a mix of urban, suburban, and agricultural areas, including the City of Lafayette and surrounding communities (Awaad et al., 2025; Saad and Habib, 2021; Saad et al., 2021). Slopes along the main stem are very mild (average slope of 1 foot for every 10 river miles or 0.0000189 m/m). As a result, the water levels are controlled by spatial variations in hydraulic head imposed by tributary inflows, wetland storage, and coastal water levels rather than a simple upstream-downstream gradient. During extreme rainfall events, floodwater moves bidirectionally toward parts of the basin that have a lower head. This causes internal division points at some locations where discharge splits in different directions, and where net flow is near zero for extended durations even while the surrounding areas remain inundated (Awaad et al., 2025). The basin contains a total of 173,327 National Structure Inventory (NSI; Gutenson et al., 2023) structures of various types (e.g., commercial, residential, industrial, educational, or government).

https://doi.org/10.5194/egusphere-2026-1388
Preprint. Discussion started: 27 March 2026

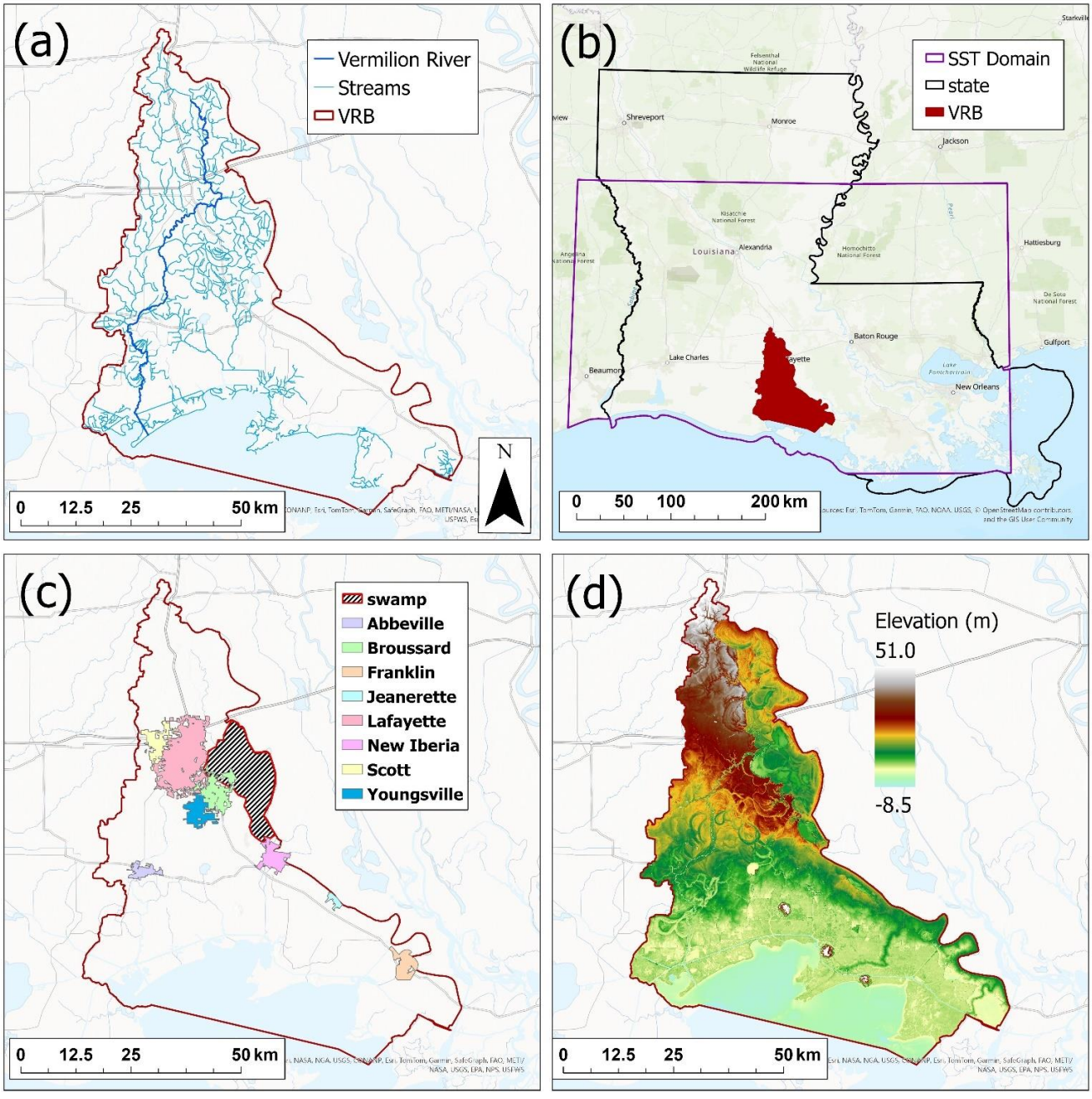

Figure 1. Spatial maps showing the different characteristics of the Vermilion River Basin (VRB). Panel (a) shows the drainage area of the VRB (redline), the main stem of the Vermilion River (dark blue line), and the basin tributaries (light blue). Panel (b) shows the SST domain used in this study (purple polygon) relative to the VRB and the state of Louisiana. Panel (c) shows the population centers in the basin (major cities), as well as the swamp area connected to the Vermilion River. Panel (d) shows the elevation in meters across the basin where low-lying flat areas such as the swamp area and the inland-coastal transition zone are depicted in dark. (Sources: Esri, NASA, NGA, USGS, CONANP, TomTom, Garmin, SafeGraph, FAO, METI, NOAA, EPA, NPS, USFWS, © OpenStreetMap contributors, and the GIS User Community. Map created using ArcGIS® software by Esri; *Powered by Esri*).

https://doi.org/10.5194/egusphere-2026-1388
Preprint. Discussion started: 27 March 2026

3 Methods

Figure 2 summarizes the overall workflow used in this study. Rainfall inputs are first defined using two alternative 100-year representations, the spatially uniform NOAA Atlas 14 deterministic storm and the spatially variable SST storm realizations, which serve as forcings to the coupled HEC-HMS and HEC-RAS (Brunner 1995) modeling framework. The hydrologic and hydrodynamic models are then run to generate gridded maximum inundation depths for each scenario. These depth rasters are then intersected with the National Structure Inventory (NSI) point layer to determine structure-specific flood depths, which are subsequently translated into structure damages using the depth-damage procedures described in Sect. 3.4. The resulting building-scale impacts are finally aggregated to produce basin-wide damage statistics that form the basis for comparing the impacts from the two design storm methods on structure damage assessment.

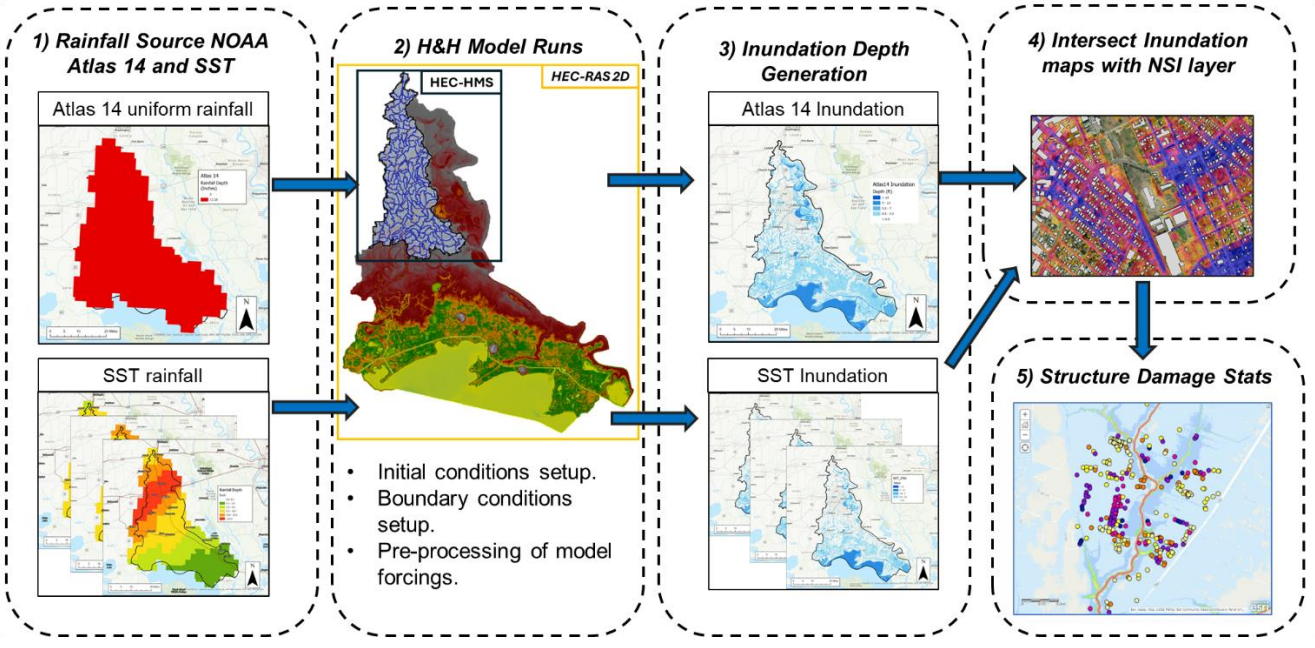

Figure 2. Workflow used to evaluate flood exposure and damage. Step (1) generates the rainfall inputs used to drive the hydrologic and hydrodynamic (H&H) models, including uniform Atlas-14–based rainfall and SST-based rainfall fields. Step (2) defines the H&H model setup, including rainfall pre-processing and specification of model initial and boundary conditions. The 2D HEC-RAS model domain (gold rectangle) covers the entire basin, while the HEC-HMS domain is shown by the black rectangle. Step (3) consists of executing the model simulations and producing SST inundation depth composites. In Step (4), the resulting inundation maps are overlaid with National Structure Inventory (NSI) building locations to calculate inundation depth and inundation frequency at each structure. Step (5) computes the damage statistics described in Sect. 3.3. (Sources: Esri, NASA, NGA, USGS, CONANP, TomTom, Garmin, SafeGraph, FAO, METI, NOAA, EPA, NPS, USFWS, © OpenStreetMap contributors, and the GIS User Community. Map created using ArcGIS® software by Esri; *Powered by Esri*).

3.1 Rainfall forcing scenarios

This study compares two distinct representations of the 100-year, 24-hour design storm over the VRB. The first is a conventional uniform storm with rainfall depths obtained from NOAA Atlas 14 (Perica et al., 2013). These rainfall depths are

https://doi.org/10.5194/egusphere-2026-1388
Preprint. Discussion started: 27 March 2026

derived from point-scale frequency analysis of historical gauge records. Although Atlas 14 is spatially distributed as gridded maps, the underlying values represent point-based depth estimates and require significant approximations to be applied to larger spatial scales (i.e., Area Reduction Factor; ARF). We obtained the 100-year, 24-hour depth from the Atlas 14 gridded product near the basin centroid and validated it against nearby rain gauge records. We then applied a depth-area adjustment following Technical Paper 40 (TP40; Hershfield 1961) to obtain an areal average consistent with the effective basin area. The basin-scale depth was then distributed temporally following an SCS Type II pattern (Khaddor et al., 2017) using the alternating-block method (Lee and Ho, 2008). The resulting rainfall hyetograph was then applied as a spatially uniform rainfall field over both the hydrologic and hydrodynamic modeling domains.

The second representation is based on Stochastic Storm Transposition (SST), which uses a long historical record of storms to construct basin-specific design storms with a desired return period. SST treats each historically observed storm as a space-time rainfall field that can be repositioned within a larger region with similar extreme-rainfall climatology. Using RainyDay (Wright et al., 2014) and the NCEP Stage IV gauge-adjusted radar rainfall archive (2002 through 2020 in this study), we identified a catalog of 'parent storms' by selecting the largest 24-hour rainfall accumulation based on rainfall accumulation occurring within the SST domain (Fig. 1, b). The SST domain is intended to cover an area with similar hydroclimatic conditions to the VRB, ensuring the transposed storms are meteorologically realistic for the target location. In addition, the domain should be large enough to contain enough parent storms to be transposed. It is important to note that identifying this domain remains an active area of research, and no exact procedure currently exists for its selection. In this study, domain selection relied on our familiarity with the study region, as well as ensuring that the majority of significant historical storms affecting the region were included in the analysis. The total number of selected 'parent storms' is based on the event-selection criterion outlined in Wright et al. (2014), which assumes a Poisson distribution for annual storm occurrences. SST realizations are then generated by repeatedly sampling a parent storm at random and transposing it within the SST domain using uniformly distributed east–west and north–south shifts. This preserves the storm's internal structure while altering its placement relative to the VRB. By repeating this procedure, we produced 50 SST realizations representing a range of plausible basin-scale 24-hour, 100-year storms.

As such, the final set of model rainfall forcing consists of one Atlas-14 uniform storm and a set of 50 SST storm realizations.

3.2. Hydrologic and Hydrodynamic Modeling Framework

To evaluate the sensitivity of flood-risk estimates to how the rainfall hazard is defined, a calibrated and verified one-way coupled hydrologic-hydrodynamic modeling framework was employed. The system was originally developed for the Louisiana Watershed Initiative (LWI) Region 5 and covers the VRB HUC-8 domain. The framework couples a semi-distributed hydrologic model (HEC-HMS V 4.11) for the upstream, high-relief portion of the VRB watershed with a two-dimensional hydrodynamic model (HEC-RAS V 6.4.1) for the lower-lying portions of the basin (Fig. 1 d and Fig. 2 step 2). Outflows from HEC-HMS serve as inflow boundary conditions for HEC-RAS. The rain-on-grid capability in HEC-RAS was used to represent

https://doi.org/10.5194/egusphere-2026-1388
Preprint. Discussion started: 27 March 2026

direct rainfall on the floodplain surface. Together, these components optimized runtime and were applied across multiple simulations to characterize flood routing and inundation behavior across the basin.

There is no significant flow contribution from neighboring watersheds, and all connections to the neighboring watersheds have hydraulic control structures. We implemented stage hydrograph time series representing the real conditions at these structures during flood events (e.g., closed gates preventing additional water from entering the basin). The domain was discretized into 187 sub-basins and 146 routing reaches where losses were estimated using the gridded deficit constant loss method, and excess rainfall was transformed to direct runoff using the ModClark method (Feldman, 2000). Runoff losses were represented using the deficit-and-constant loss method, with parameters derived from Soil Survey Geographic Database (SSURGO; Mikhailova et al., 2016) soils data and adjusted for land development and imperviousness. Excess precipitation was transformed to runoff using the ModClark method to capture distributed watershed response while maintaining computational efficiency. During calibration, loss and ModClark timing parameters were adjusted to improve runoff volume and hydrograph timing, after which a consistent parameter set was applied across events with event-specific initial deficit values. Baseflow was simulated with the recession method, and channel routing was performed using the Muskingum-Cunge approach (Ponce and Yevjevich 1978). Calibration and validation were conducted against a total of eight historical flood events, covering both tropical and non-tropical events. Performance was evaluated using the Nash–Sutcliffe Efficiency (NSE; McCuen et al., 2006), along with peak-discharge and total-volume error metrics. The resulting runoff hydrographs were used as boundary inflows to the 2D hydrodynamic model.

Floodplain inundation was simulated using HEC-RAS version 6.4.1 with the rain-on-grid configuration. The 2D model domain covers approximately 3,626 km² (1,400 mi²), including the Vermilion River main stem and the associated floodplain. An unstructured mesh was used, with characteristic cell sizes of ~90 m (300 ft) in rural areas and 15-30 m (50-100 ft) in urbanized or hydraulically constrained reaches. The terrain model was constructed from USGS QL2 (or higher) LiDAR-based Digital Elevation Model (DEM), supplemented with channel bathymetry from single-beam sonar surveys to maintain cross-sectional integrity and capture backwater-affected low-gradient flows. Spatially distributed Manning's n values were derived from the 2019 NLCD (Dewitz, 2021), with localized adjustments in engineered or vegetated corridors. Calibration regions were applied to refine roughness in stream channels and Vermilion Bay, with adjustments guided by channel width, aerial imagery, and site conditions. During calibration, roughness values were adjusted to improve hydrograph timing and shape, while maintaining physically reasonable ranges. The final calibrated roughness values were fixed for validation events and provided consistent performance across all simulated storms. More than 615 bridges, culverts, and other hydraulic structures were explicitly represented based on detailed survey data. Rainfall was applied through rain-on-grid, and model behavior was confirmed against USGS water-surface elevations and high-water marks from events including Hurricanes Laura (2020) and Delta (2020). Model calibration and verification were assessed using the Pearson product–moment correlation coefficient (PPCC), standardized RMSE (%), and percent bias (PBIAS) for both stage and flow. Performance targets required PPCC values greater than 0.9 for stage and greater than 0.7 for flow, while RMSE (%) and PBIAS were used to evaluate overall error magnitude and systematic bias. For each event, model performance was considered acceptable when at least 50 percent of the evaluated

https://doi.org/10.5194/egusphere-2026-1388
Preprint. Discussion started: 27 March 2026

gages met the criteria for each metric. For readers seeking complete model data, metadata, terrain files, and output maps from the watershed-scale applications, the "Louisiana Watershed Initiative" (LWI) maintains a publicly accessible digital repository, the Environmental Data and Model Catalog (EnDMC; LWI 2025).

All 51 simulations (NOAA Atlas-14 and 50 SST-based events) were run with identical hydrologic and hydraulic boundary conditions so that differences in results reflect only the rainfall specification. Initial soil moisture conditions in both HEC-HMS and HEC-RAS were set to 36.8% of maximum storage to represent intermediate antecedent conditions. Sensitivity tests indicated that, at rainfall magnitudes associated with the 100-year storms, variations in antecedent wetness had a limited influence on peak inundation, reinforcing the conclusion that rainfall definition was the controlling factor in scenario-to-scenario differences.

Upstream inflows were generated by running HEC-HMS with the gridded rainfall fields prepared for each of the 51 events. The resulting runoff hydrographs were then used as inflow boundaries to the 2D HEC-RAS model. At the downstream boundary along the Gulf Intracoastal Waterway, a dynamic tidal signal was imposed, parameterized using mean higher-high water (MHHW) and mean lower-low water (MLLW) conditions informed by records from the Charenton Drainage Canal and USGS Station 07387040. The resulting stage hydrograph at the coastal boundary condition represents the mean tidal cycle during average gulf conditions and was applied for all simulations to ensure consistency and that the downstream boundary condition is not a major factor in determining flood extent or magnitude.

3.3. Consequence Assessment and Statistical Analysis

3.3.1. Consequence Modeling Engine and Structure Inventory

Structure damage analysis was conducted using Go-Consequences (Gutenson et al., 2023), a lightweight USACE consequence modeling engine designed for large event ensembles. For each rainfall scenario, maximum inundation depth layers from the hydrodynamic simulations were intersected with point locations from the National Structure Inventory (NSI) v2.0 (Gutenson et al., 2023). The NSI contains key building attributes, including occupancy class and structure value, and most importantly, it includes first-floor elevation and foundation type, which are key in determining if structural damage will occur for a given flood depth.

Flood depth at each structure was computed as:

$$\mathrm{Depth}_i = \max(0, \mathrm{h}_i - \mathrm{FFE}_i) \quad (1)$$

where h_i is the simulated water-surface elevation at the structure i, and FFE is its first-floor elevation. Using depth relative to first-floor elevation, monetary losses due to structural damage were computed as a fraction of each building's replacement value and then aggregated to produce basin-wide damage totals for each event.

https://doi.org/10.5194/egusphere-2026-1388
Preprint. Discussion started: 27 March 2026

3.3.2. Statistical and Spatial Analysis of Risk Divergence

To evaluate how the choice of storm representation drives divergence in flood impacts, we conducted a suite of statistical and spatial analyses linking differences in rainfall spatial distribution to differences in inundation depth, the number of affected buildings, and associated monetary losses across the 51 mode simulations driven by Atlas-based and SST storms. The analysis proceeds in four main components:

(a) Distributional analysis of inundation depths: For all inundated buildings in each scenario, depth distributions were analyzed using empirical density functions and fitted lognormal parameters (μ_{ln}, σ_{ln}). These distribution parameters allow comparison of both central tendency and upper-tail behavior, highlighting how spatial rainfall variability alters typical depths.

(b) Basin-wide and per-building loss divergence: Total economic losses were compared across the Atlas-14 event and the SST distribution. Depth-damage outputs were aggregated to compute the ensemble distribution of basin-wide losses, enabling direct quantification of whether Atlas-14 corresponds to median, upper-decile, or maximum outcomes within the SST ensemble.

(c) Exposure gap identification: To identify structures whose flood susceptibility depends on the spatial organization of rainfall (SST storms) rather than basin-wide uniform rainfall (Atlas-based storm), we quantified the exposure gap, defined as the set of buildings inundated under at least one SST realization but never inundated under the Atlas-driven simulation. For each building i, inundation was represented as a binary indicator for every rainfall scenario s:

$$I_{i,s} = \begin{cases} 1 \; if \; building \; i \; experienced \; positive \; inundation \; depth \; under \; scenario \; s; \\ 0 \; otherwise. \end{cases} \quad (2)$$

Let S_{SST} denote the set of all SST realizations and let A denote the Atlas-14 storm. A building was classified as belonging to the SST-exclusive exposure group if:

$$I_{i,A} = 0 \; and \sum_{s \in S_{SST}} I_{i,s} > 0. \quad (3)$$

For each SST-exclusive structure, the inundation frequency was computed as

$$F_i = \sum_{s \in S_{SST}} I_{i,s} \quad (4)$$

where F_i represents the number of SST realizations (out of the full ensemble) in which building i was inundated. This measure provides a scenario-normalized indicator of how often structures become exposed only when storms are represented with variable spatial rainfall using SST. Frequencies were summarized for all SST-exclusive structures using empirical distributions.

For each SST-exclusive building, we collected all inundation depths across the SST ensemble and used that sample to describe both flood depth ranges for that structure. Structural damages were then computed for every realization using the depth–

https://doi.org/10.5194/egusphere-2026-1388
Preprint. Discussion started: 27 March 2026

damage procedure in Sect. 3.4.1, and for each SST storm, we summed the resulting losses across all SST-exclusive buildings (i.e., not inundated by Atlas-14 storm) to obtain their projected total loss.

(d) Spatial analysis of cluster intensification and topographic sensitivity: Spatial patterns of inundation were characterized using a two-component analysis that combined Kernel Density Estimation (KDE) of inundated structures with terrain information derived from Height Above Nearest Drainage (HAND; Nobre et al., 2011). The purpose of this analysis was to obtain a consistent, quantitative description of flood clustering and to understand the causes of these buildings' sensitivity to spatial variability in storm representations.

KDE was applied to the centroids of inundated buildings to obtain a smooth representation of cluster intensity. Let the locations of inundated structures be $x_1, x_2, \ldots, x_n$, with x_i in $\mathbb{R}^2$. The estimated density at the location x was computed as:

$$\hat{f}(x) = \frac{1}{n\,h^2} \Sigma\, K\left(\frac{||x - x_i||}{h}\right) \quad (5)$$

where K(.) is a Gaussian kernel and h is the bandwidth that controls the degree of spatial smoothing. A single kernel form and a single bandwidth were used for all the evaluated flood maps. These KDE surfaces provide a quantitative basis for comparing the intensity and extent of inundation clusters across hazard definitions.

Topographic characteristics of different locations relative to inundation potential were represented using the HAND method. For each elevation cell (3 m x 3 m), HAND was computed as:

$$HAND(x) = z(x) - Z_{drain}(x) \quad (6)$$

where z(x) is the ground elevation at the location x, and $Z_{drain}(x)$ is the elevation of the nearest hydrologically connected drainage cell along the flow network. HAND measures the vertical distance that must be filled before flow is routed toward the channel, and it is used as a terrain-based proxy for relative flood susceptibility. HAND values were extracted at all inundated building locations. The distribution of HAND among inundated structures was summarized using 1 m histogram bins and empirical cumulative distribution functions. This provides a consistent way to identify elevation bands where inundation is most sensitive to the spatial distribution of rainfall.

4. Results

Comparison of the deterministic NOAA Atlas 14 100-year storm with SST-based storm realizations revealed clear differences in inundation patterns. To facilitate this comparison, five composite inundation maps were generated from the SST ensemble: the 25th percentile (P25), median (P50), 75th percentile (P75), 90th percentile (P90), and maximum (SST_{max}) inundation depth across all realizations. These composites, together with the Atlas-14 inundation, were intersected with the NSI dataset to quantify building-level inundation depths and associated structural damages as described in Sect. 3.3.2.

https://doi.org/10.5194/egusphere-2026-1388
Preprint. Discussion started: 27 March 2026

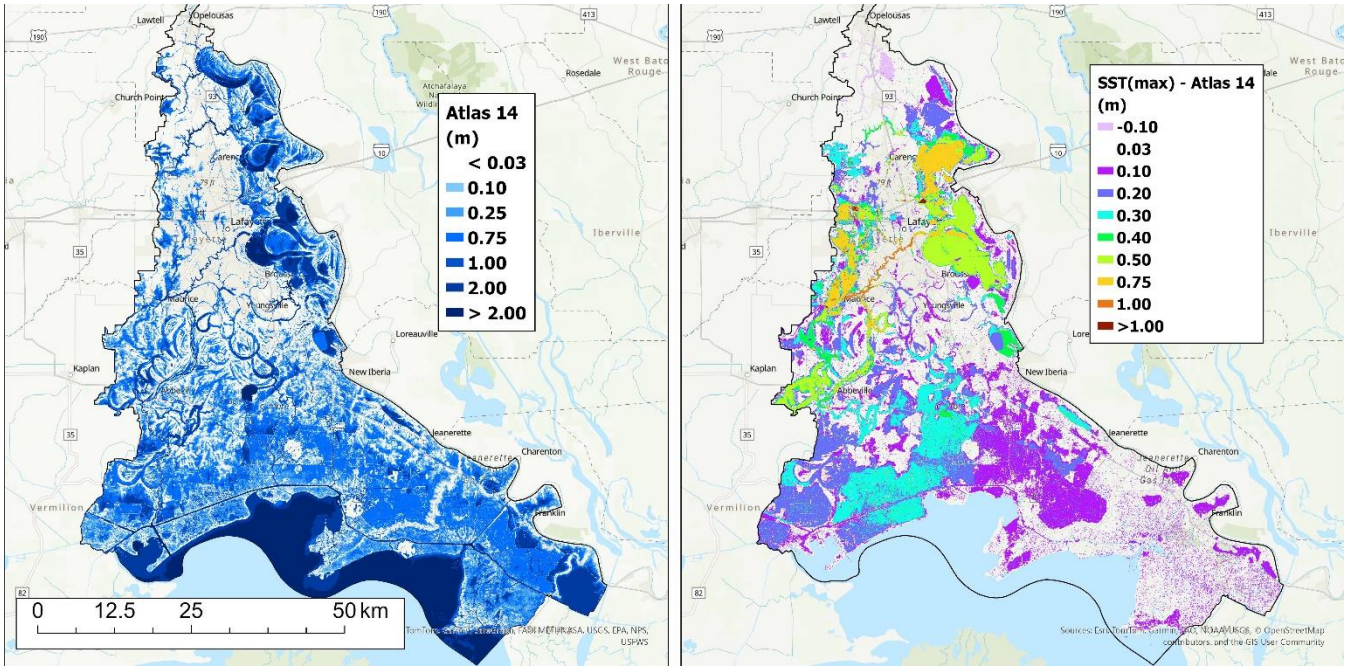

Figure 3. Spatial maps showing the basin-wide inundation depths produced by the NOAA Atlas-14 design storm (left panel) and the depth differences between SST maximum composite (SST_{max}) relative to Atlas-14 (SST_{max}-Atlas-14; right panel). (Sources: Esri, NASA, NGA, USGS, CONANP, TomTom, Garmin, SafeGraph, FAO, METI, NOAA, EPA, NPS, USFWS, © OpenStreetMap contributors, and the GIS User Community. Map created using ArcGIS® software by Esri; *Powered by Esri*).

Figure 3 shows the impact of storm representation on the modeled flood depth and extent. The Atlas-14 simulation inundates a significant portion of the VRB, with widespread inundation in the southern part of the basin where depths reach up to 2 m in some locations. Inundation along the upstream tributaries is relatively shallower but more consequential due to their proximity to populated areas. The difference map highlights where the spatially variable SST rainfall generates deeper or shallower flooding than that resulting from the spatially uniform Atlas-14 rainfall. Positive differences occur in areas where SST produces higher inundation depths, while negative differences denote locations where Atlas-14 exceeds the SST Maximum. The majority of the differences in inundation depth occur in unpopulated areas near the Gulf Coast, while the largest difference in terms of magnitude occurs within the banks of the northern portion of the Vermilion River (Fig. 1 a) and the swamp area (Fig. 1 c) connected to it. As described in Awaad et al. (2025), this part of the river experiences complex flow regimes during extreme events such as reverse flows moving upstream towards the swamp area. In this study, however, we focus on population centers where changes in inundation depth translate directly into changes in structural damage. The most prominent positive differences at populated locations occur in the west-central portion of the basin near Lafayette-Scott and throughout the city of Abbeville region in the southwest (Fig. 1 c), where the difference in inundation ranged from 0.3 to 0.75 meters. Another notable populated location with significant inundation difference is the city of New Iberia, located in east-central VRB, with inundation differences ranging from 0.1 to 0.5 meters.

https://doi.org/10.5194/egusphere-2026-1388
Preprint. Discussion started: 27 March 2026

4.1 Distribution of Inundation Depths

Figure 4 presents the distribution of inundation depths for the Atlas-14 simulation and for each SST composite. Across all scenarios (Atlas-14 and the different SST composites), the depth distributions are strongly right-skewed, characterized by numerous shallow inundations and a progressively thinner upper tail. This form is consistent with the lognormal curves fitted to each scenario, whose corresponding parameters (μ_{ln}, σ_{ln}) are displayed in their respective panels. These parameters provide a summary of the distributional behavior and reveal two important patterns.

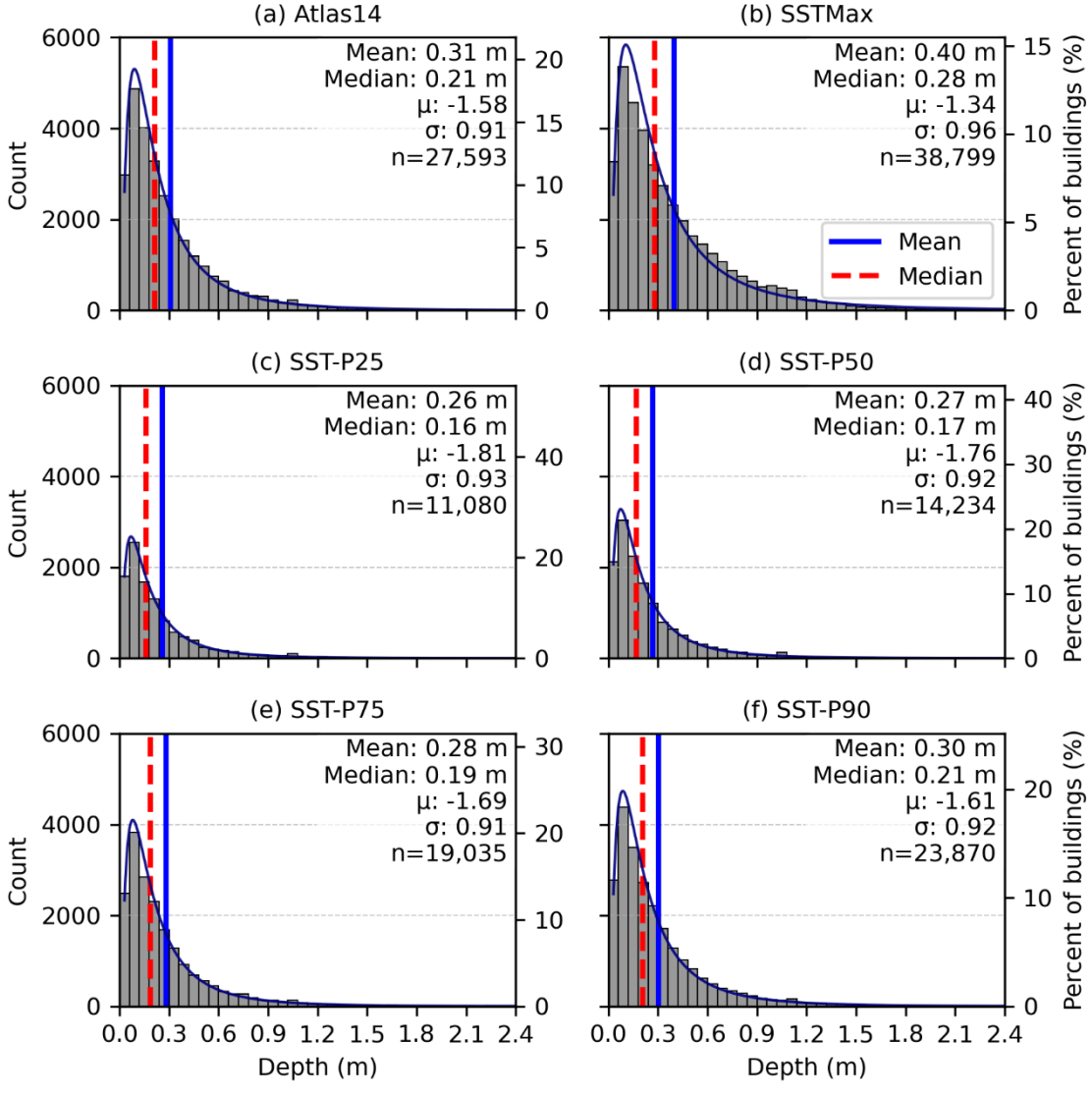

Figure 4. Histograms showing the distribution of inundation depths derived from the uniform rainfall-based inundation map (a) and from SST-based composite inundation maps (b through f). Each panel shows the median inundation depth (vertical red dashed line) and mean depth (vertical blue line). The fitted log-normal distribution parameters and the number of inundated buildings (n)

https://doi.org/10.5194/egusphere-2026-1388
Preprint. Discussion started: 27 March 2026

are also reported in each panel. The SST composite scenarios include SSTmax (b) and composites corresponding to the 25th, 50th, 75th, and 90th percentiles (c through f), respectively.

First, the shape parameter σ_{ln}, which represents the dispersion of the depths, is stable across all scenarios. In the Atlas-14 case and in each of the SST percentile composites, σ_{ln} varies only modestly, indicating that the relative spread between shallow and deep inundation is largely governed by the basin's topography rather than by a specific storm realization. The stability of σ_{ln} suggests that while a storm's spatial variability can change how many buildings flood or how deep the inundation can get at these locations, it does not fundamentally alter the underlying relative differences in flooding potential across the basin.

Second, the location parameter μ_{ln}, which controls the central tendency of the lognormal distribution, shifts noticeably across the scenarios. Atlas-14 produces a distribution centered around μ_{ln} values consistent with a median depth near 0.2 meters, reflecting broad but relatively uniform inundation (i.e., no disproportionate concentration of impact areas). The SST percentile composites P75 through P90 produce values that closely track those of Atlas-14, indicating that many SST realizations generate storms whose basin-wide impacts, in terms of flood severity, resemble those of Atlas-14.

In contrast, the SST_{max} composite displays a substantially higher μ_{ln} value, corresponding to a median depth near 0.3 meters and a visibly heavier upper tail. This upward shift in μ_{ln} is not caused by differences in total storm volume or basin storage, but by localized high-intensity rainfall features that occur in a subset of SST realizations. This is because the average basin rainfall accumulation across all SST realizations is 238.0 mm, while the uniform Atlas-14 depth after TP40 reduction is 310.0 mm. Thus, it is likely that spatially concentrated rainfall cores produce deeper inundation, increasing the central tendency of depths and expanding the upper tail beyond what the uniform deterministic storm produced.

These μ_{ln} and σ_{ln} patterns highlight that the shape of the depth distribution is mostly topographic (i.e. vulnerable locations will flood from both types of storms), while the location and upper-tail behavior are strongly influenced by the spatial distribution of rainfall. Atlas-14 suppresses upper-tail variability due to its spatial uniformity, whereas SST introduces the small-scale variability necessary for revealing additional vulnerable locations that are not impacted under the Atlas-14 scenario.

4.2 Divergence in Aggregate Losses

Figure 5 summarizes flood impacts in terms of (a) inundation depth, (b) per-structure loss value, USD, and (c) basin-wide aggregate impact both in structure numbers and loss in value. These panels demonstrate two important aspects of the relationship between storm choice and economic losses.

https://doi.org/10.5194/egusphere-2026-1388
Preprint. Discussion started: 27 March 2026

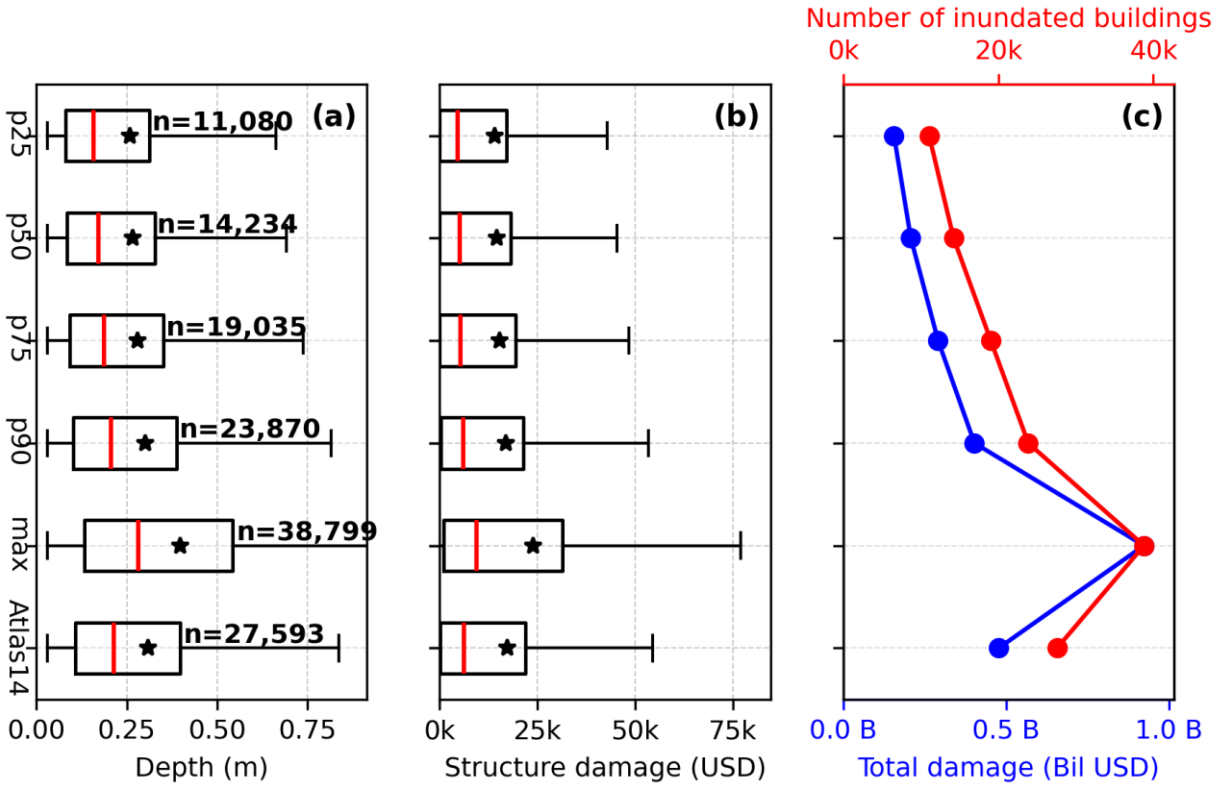

Figure 5. Box plots of flood depth (a) and structure damage (b) across all inundation scenarios. Black stars indicate the mean and the red line within each box indicates the median; n denotes the number of inundated buildings. Panel (c) shows total estimated damage (billions USD; blue line, bottom x-axis) and the total number of inundated buildings (red line, top x-axis).

First, the uniform Atlas-14 rainfall results in a high-severity outcome comparable to upper-percentile SST composites (P75 and P90). The total structural damage produced by Atlas-14 (approximately $0.48B) slightly exceeds that of the SST's 90th percentile (P90), indicating that Atlas-14 accounts for most potential basin-wide losses.

Second, even though Atlas-14 aligns with the upper decile of the SST composites, it does not capture the highest plausible losses (middle and right panels). For example, the SST_{max} scenario produces damages approaching $0.8B (panel (c), blue line), substantially exceeding both the Atlas-14 estimate and the bulk of the SST distribution. This divergence in the total number of impacted buildings is due to localized rainfall intensities occurring over densely developed areas, a condition that the spatially uniform rainfall cannot capture. In other words, a uniform storm mimics a widespread severe storm, but it cannot represent the spatially concentrated rainfall patterns that generate the heavy-tail of the loss distribution. While the major increase in loss value is attributed to both the overall increase in total number of impacted buildings as well as the increase in the average depth per building location as depicted in Fig.5, the spatial difference map (Fig. 3, right panel) shows that there is a concentration of high differences in flood depths in a highly populated area (i.e., Lafayette-Scott area) which have contributed

https://doi.org/10.5194/egusphere-2026-1388
Preprint. Discussion started: 27 March 2026

significantly to this divergence. This observation emphasizes how localized extreme rainfall over highly populated areas can elevate the overall risk profile for the entire basin.

4.3 Quantifying the Exposure Gap

Next, we identified the structures that were inundated in at least one SST realization but were unimpacted under Atlas-14. This highlights the relative risk of the vulnerable structures that Atlas-14 misses. Figure 6 summarizes this exposure gap, including both the number of impacted structures and their corresponding inundation depth and losses.

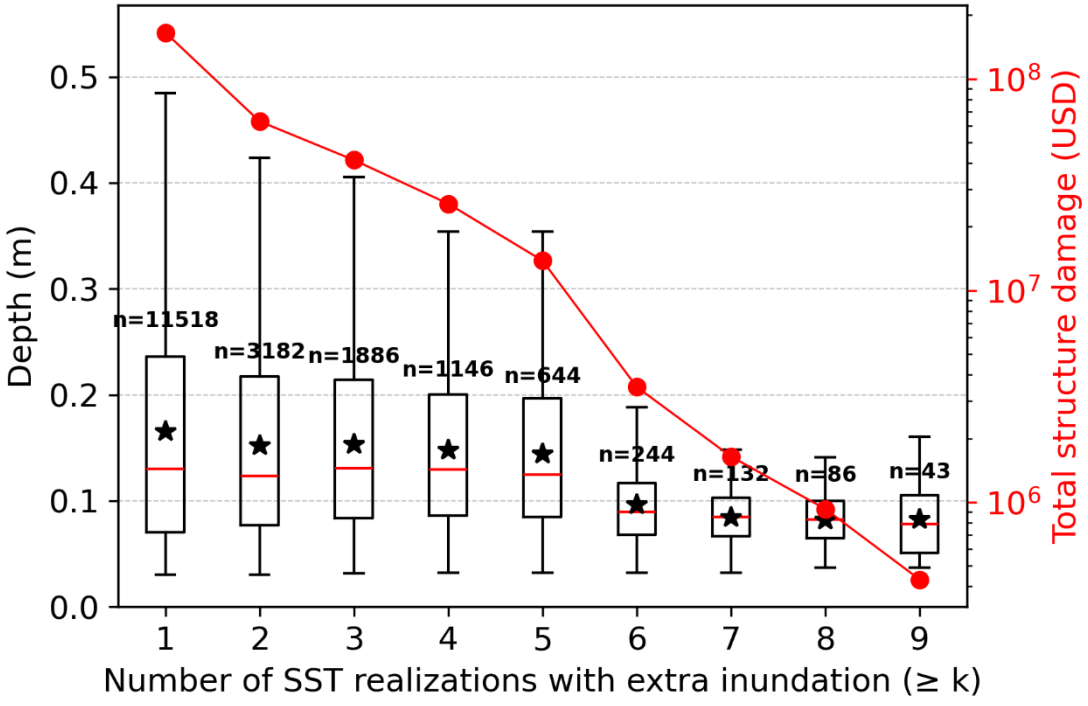

Figure 6. Depth metrics and aggregate damage estimates based on the number of times a set of structures was inundated by SST realizations but not by Atlas-14, occurring at least k times. Inundation depths are shown using box plots (left y-axis, black), where the solid black star represents the mean depth and the red line within each box represents the median depth. The total number of inundated buildings included in each box is shown as (n). Total structure damage for each group is represented by solid red dots (right y-axis, red).

This gap includes 11,518 impacted structures that were not impacted in the Atlas-14 scenario. A relatively significant portion of the unimpacted structures were inundated in one to four SST realizations (>1000 structures), with the frequency decreasing sharply beyond that point. This indicates that a large portion of this gap gets inundated only under specific storm placement conditions that have a relatively low occurrence probability out of the 50 analyzed realizations.

The inundation depths for these structures are significant (median depths between 0.08 and 0.13 meters), resulting in a significant amount of potential losses and cumulative structural losses of up to ~$110M for this SST-exclusive impacted group of structures.

https://doi.org/10.5194/egusphere-2026-1388
Preprint. Discussion started: 27 March 2026

4.4 Spatial Intensification of Inundation Clusters

So far, we have characterized the differences between Atlas-14 and SST in terms of inundation depth, number of impacted structures, and the monetary value of structure losses. Here, we expand our investigation by identifying the special distribution and the specific locations where disproportionate impacts occur. Figure 7 compares the spatial density of inundated buildings under the Atlas-14 and SST_{max} scenarios using KDE clustering analysis as described in Sect. 3.4.2. The cluster patterns show that while both approaches succeed in outlining the main low-lying (Fig. 1 d) flood-susceptible regions, two areas show significantly stronger impacts under SST_{max}. Namely, the most significant difference in cluster sizes occurs at the relatively densely populated areas of Lafayette-Scott and Abbeville. In the case of Atlas-14, KDE clusters are visible at these locations; nevertheless, they are relatively moderate in both size and intensity. Under SST, the same locations exhibit substantially more concentrated, higher-intensity clusters, indicating a greater number of impacted structures. This is a strong indication that these areas are relatively more sensitive to localized storm intensification compared to the remainder of the VRB. This clustering pattern is in agreement with the spatial distribution of inundation depth differences as observed in Fig. 3; nevertheless, there are other locations that have similar inundation depth difference patterns that did not experience the same increased intensity of impacted structures (e.g., the heavily populated areas around the main stem of the Vermilion River west and south of the city of Lafayette). Thus, this discrepancy in cluster sizes warranted additional investigation to determine the potential underlying cause of this phenomenon.

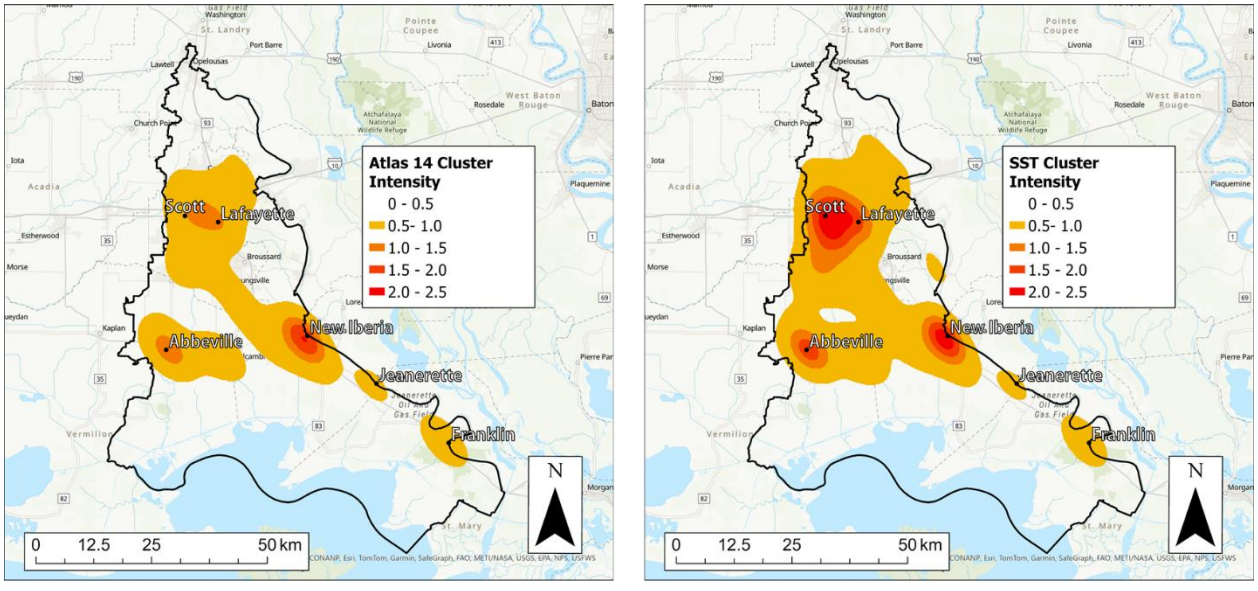

Figure 7. Spatial maps showing KDE Clustering analysis of structure inundation impacts for Atlas-14 (left) and SST max (right). (Sources: Esri, NASA, NGA, USGS, CONANP, TomTom, Garmin, SafeGraph, FAO, METI, NOAA, EPA, NPS, USFWS, © OpenStreetMap contributors, and the GIS User Community. Map created using ArcGIS® software by Esri; *Powered by Esri*).

https://doi.org/10.5194/egusphere-2026-1388
Preprint. Discussion started: 27 March 2026

4.5 Relationship Between Cluster Intensification and HAND

To investigate the underlying drivers of the intensified SST_{max} clusters, we visually inspected various topographic and drainage network characteristics at these locations. The topographic variables we investigated included elevation and slope, while the drainage network characteristics included the total number and size of the surrounding drainage channels and the proximity of the structures to the channels. Additionally, we quantified the total number of buildings in these areas and compared them to other densely populated areas of the VRB. This visual inspection pointed towards a consistent spatial pattern where the differences in cluster intensities tended to occur in neighborhoods situated neither in the low floodplain elevations, which flooded similarly under both the Atlas-14 and the SST_{max} scenarios, nor in high terrain areas that rarely flooded under either scenario. Instead, the discrepancies appeared to be concentrated in intermediate elevation zones located along the transition between low floodplain areas and upland terrain. Additionally, the size and depth of the channels draining those areas were relatively modest. These observations suggested that local HAND values can directly explain where local intensification of rainfall variability most strongly alters inundation patterns. To evaluate this hypothesis, we calculated the HAND (Fig. 8) surface as described in Sect. 3.4.2.

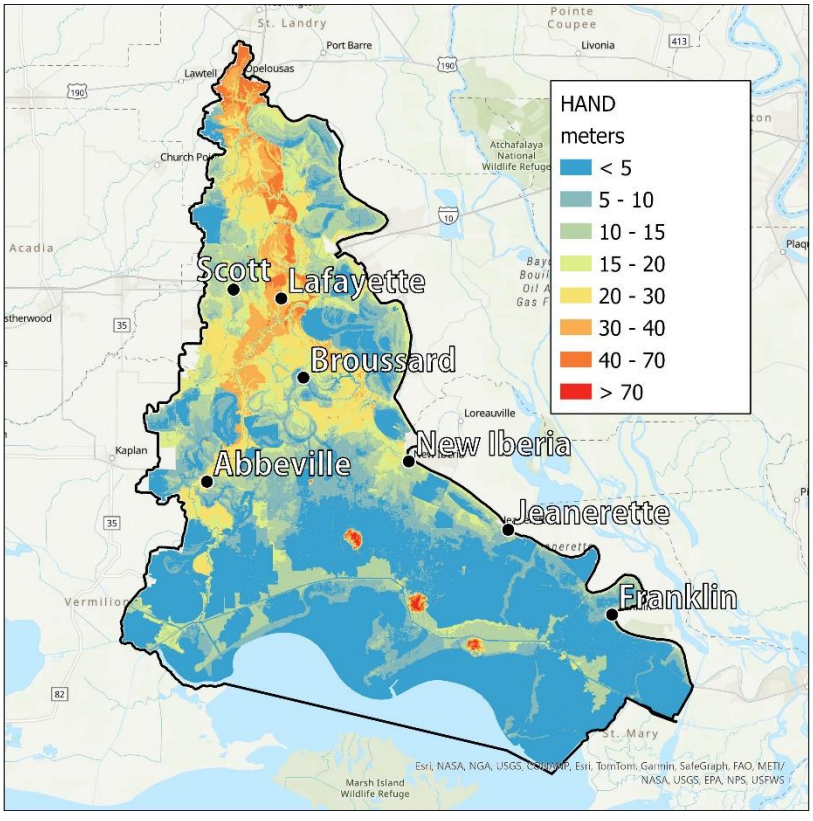

Figure 8. A spatial map depicting the calculated HAND distribution for the VRB. (Sources: Esri, NASA, NGA, USGS, CONANP, TomTom, Garmin, SafeGraph, FAO, METI, NOAA, EPA, NPS, USFWS, © OpenStreetMap contributors, and the GIS User Community. Map created using ArcGIS® software by Esri; *Powered by Esri*).

https://doi.org/10.5194/egusphere-2026-1388
Preprint. Discussion started: 27 March 2026

Figure 8 shows that the lowest HAND values (light blue) delineate the primary floodplain flat areas, such as inland-coastal zones in the south, as well as swamp areas near the east-central portion of the VRB, as well as shallow wetlands across the basin. Mid-range HAND values between 10 and 30 m (green to yellow hues) occupy extensive areas in and around West Lafayette, Scott, Abbeville, and portions of New Iberia. Higher HAND values (orange hues) mainly cover the portion of the areas immediately surrounding the main stem of the Vermilion River, starting north of the city of Abbeville and extending further north past the city of Lafayette. Visual comparison between Fig. 8 and the spatial distribution of SST_{max}-Atlas-14 inundation depths (Fig. 3, top right corner) confirms that the most substantial positive differences (i.e., SST_{max} depth > Atlas-14 depth) at populated areas occur within these mid-range HAND-dominated zones.

In Fig. 9, we further examine the association between HAND and the increase in the number of structures impacted by plotting the number of inundated structures for each HAND value. The gray bars represent buildings inundated under Atlas-14 within each 1-meter HAND interval, while the red bars represent buildings inundated under SST_{max} only. The blue curve is the Cumulative Density Function (CDF) of the number of Atlas-14 inundated structures, while the red curve is the CDF of the SST_{max}-Atlas difference set (SST_{max} only).

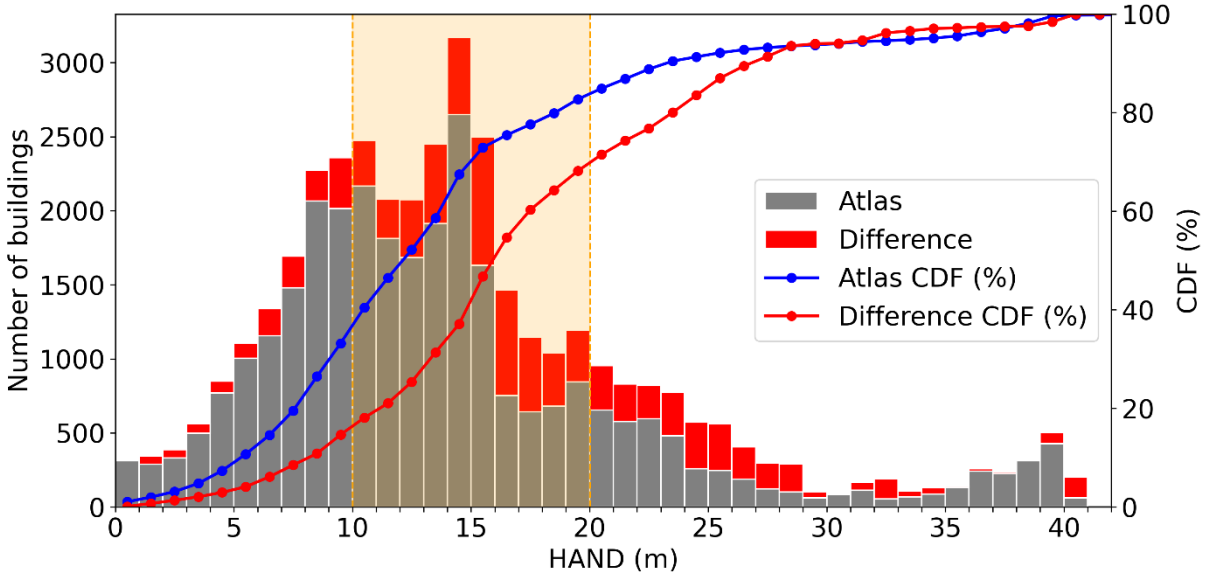

Figure 9. Bar chart showing the number of inundated buildings across HAND values. Gray bars represent the buildings that were inundated during the Atlas-14 scenario. The red bars represent the buildings that were inundated during the SST max scenario but not Atlas-14. CDF for Atlas-14 and SST-Atlas-14 are represented by the blue and red lines, respectively. The orange shaded area represents the HAND interval responsible for the middle 60% of SST-Atlas divergence.

As expected, the Atlas-14 CDF rises rapidly at low HAND values and reaches approximately 75 percent of its inundated structures near HAND value of 15 meters, after which it starts to level off. This is because uniform rainfall predominantly floods the relatively highly vulnerable portions of the landscape while having less impact on structures situated at higher HAND elevations. On the other hand, the difference CDF (red) begins to significantly increase near HAND value of 10 meters,

https://doi.org/10.5194/egusphere-2026-1388
Preprint. Discussion started: 27 March 2026

then rises steadily through mid-range HAND values, and does not flatten until approximately a HAND value of 28 meters. This demonstrates that the disagreement between two CDFs is concentrated in the intermediate HAND range, where buildings lie near their potential inundation thresholds and are sensitive to local flooding caused by concentrated rainfall clusters.

To quantify this sensitivity, we computed the area between the two CDFs and identified the HAND interval responsible for the middle 60% of SST-Atlas divergence (Figure 9, orange shaded area). This interval lies between HAND values of 10 and 20 meters. Notably, this HAND range aligns closely with the typical HAND values in the Lafayette-Scott and Abbeville neighborhoods highlighted in Fig. 8. Thus, based on this investigation, we conclude that the KDE cluster intensification seen in Fig. 7 can be directly explained by the HAND CDF differences shown in Figure 9.

5. Discussion

In this study, we examined how the storm representation influences the modeled flood depth and extent, as well as the resulting losses to exposed structures. Although deterministic, spatially uniform Atlas-14-based storms are widely accepted as the current state of practice in flood risk mapping, the effects of applying this simplified rainfall representation on flood risk and structural losses are underexamined. By comparing the inundation produced by the Atlas-14-based storm with that from an ensemble of 50 SST-based storm realizations, we identified areas with underestimated risk potential. We also investigated the topographic characteristics that contribute to amplifying the risk potential when spatial rainfall variability is accounted for.

The results of the comparison showed clear differences in inundation depth, extent, and basin-wide economic loss estimates. Across all rainfall scenarios (i.e., Atlas-14 vs. SST percentile-based composites), the depth distributions for the inundated buildings were strongly right-skewed and well approximated by lognormal fits, with similar shape parameters across scenarios. The location parameter for Atlas-14 was comparable to that of the SST 90th-percentile composite, while the maximum SST composite had a higher median depth and a thicker upper tail. Basin-wide losses were consistent with this pattern, where the Atlas-14 scenario resulted in approximately 0.48 billion USD in damages, while the SST percentile-based composites spanned a wider range, reaching nearly 0.8 billion USD in the case of the SST_{max} composite. The SST realizations also identified 11,518 structures that were inundated at least once but were dry under the Atlas-14 scenario. This difference highlighted an additional cumulative damage exceeding ~$110 million USD. Moreover, spatial clustering analysis showed that SST_{max} consistently produced wider and more intense damage clusters, particularly within some developed population centers.

The similarity between Atlas-14 and the SST 90th-percentile composite reflects the smoothing effect introduced by how percentile composites are generated. This is because SST 90th-percentile per pixel calculation acts as a low-pass filter applied to the full ensemble of flood inundation maps obtained from all SST realizations. It preserves the flood patterns that appear consistently across the ensemble while suppressing the low-frequency inundation pockets that occur only under the most extreme localized rainfall. Meanwhile, SST_{max} retains the full extent and severity of inundation associated with the localized extreme rainfall, producing higher median depths, a thicker upper tail, and intensified damage clusters in areas that are not typically regarded as highly vulnerable but nevertheless become exposed under intense localized rainfall. The Basin-wide

https://doi.org/10.5194/egusphere-2026-1388
Preprint. Discussion started: 27 March 2026

HAND analysis reinforces this interpretation by showing that the largest discrepancies occur in mid-elevation areas that are not directly considered part of the floodplain in any scenario. Merz et al. (2008) stated that in flood risk assessment, uncertainty in depth-damage calculations is more impactful during low-intensity events, while uncertainties in flood frequency analysis dominate during rarer events. Our results add to this by demonstrating that simplified design storm representation introduces systematic bias in flood risk estimation. This aligns with Wing et al. (2022), who showed that deterministic, spatially uniform flood hazard maps do not cover a substantial fraction of flood-prone areas. Our findings are also consistent with Gutenson et al. (2023) and Grimley et al. (2025), who showed that estimates of flood exposure and damage can change significantly depending on how the contributing flood drivers are represented. Wright et al. (2025) argued that hydrologic prediction requires ensemble-based representations of rainfall fields because deterministic rainfall inputs cannot resolve the spatial and temporal uncertainty inherent in rainfall observations. In this study, we add to this body of literature by showing that the common practice of representing frequency-based storm scenarios as deterministic and spatially uniform events can underestimate flood risk within a study area, and we demonstrate how basin characteristics interact with deterministic and stochastic rainfall representations, leading to differences in estimated flood risk.

A few limitations of the analysis should be noted. This study compares two interpretations of the 1% annual exceedance probability design stormSST and Atlas-14-based uniform design storms). Although different in nature, these representations only represent one class of flood risk drivers, namely, inland rainfall. There are, however, other representations that include, for example, different types of coincident flood drivers such as storm surge-rainfall combinations associated with tropical systems, or the compounding effects of spatial or temporal storm clustering (Amorim et al., 2025; Liu et al., 2025; Grimley et al., 2025). Nevertheless, our focus in this study is limited to highlighting how the choice of design storm can impact structure loss estimates. Another limitation of this work is the computational cost of the modeling approach. The coupled HEC-HMS/HEC-RAS model used in this study provides a detailed representation of channels, hydraulic structures, and storage areas, which is needed to simulate complex flood regimes within the watershed. This level of detail comes at a computational cost and restricts the number of simulations that can be executed in a reasonable timeframe. Merz et al. (2008) also discussed the problem of computational costs in the hydrologic sciences and how they limit practitioners' ability to conduct ensemble-based analyses. Fifty SST realizations, therefore, reflect a computational upper bound rather than all possible 100-year design storms that can be generated using the SST approach. According to Wright et al. (2014) and Zhu et al. (2018), fifty realizations are sufficient for their applications similar to ours, and Zhu et al. (2018) noted that 20 realizations produced variability comparable to that obtained from 50 realizations. Simpler models such as SFINCS (Grimley et al., 2025) allow for hundreds or thousands of simulations in a reasonable amount of time; however, they do so by simplifying or completely omitting representations of hydraulic controls, storage areas, and channel bathymetry, which are important features for our application, especially in low-gradient watersheds such as the VRB.

https://doi.org/10.5194/egusphere-2026-1388
Preprint. Discussion started: 27 March 2026

6 Conclusions

This study evaluated how the choice of design storm representation affects structure flood damage estimates in the Vermilion River Basin (VRB), south Louisiana. By comparing a conventional, the deterministic, spatially uniform NOAA Atlas 14-based design storm against 50 stochastic storm transposition (SST) realizations, we quantified the effects of rainfall spatial variability on inundation mapping (i.e., depth and extent) and monetary structural damage assessment. The analysis highlighted systematic exposure gaps and damage underestimation that occur when spatially uniform design storms are applied to a low-gradient, hydrologically complex watershed. The study's main findings can be summarized as follows:

1. Flood exposure can be underestimated when frequency-based storm scenarios are represented as deterministic and spatially uniform events instead of stochastic rainfall realizations. In the VRB, the SST ensemble identified 11,518 structures that were inundated by at least one SST realization but remained dry under the Atlas-14 storm, corresponding to approximately $110 million in potential losses that would otherwise be overlooked.
2. Flood severity can also be underestimated when localized rainfall variability is ignored, as spatially uniform storm representations suppress the upper tail of the flood depth distribution where the largest losses occur. In the VRB, this resulted in losses approaching $0.8 billion under the SSTmax composite compared to $0.48 billion estimated using the Atlas-14 storm.
3. Clustering analysis showed that the SST storms systematically increased the intensity and extent of damage clusters in some major population centers while having little to no impact on other population centers. By further examining the spatial distribution of these differences using Height Above Nearest Drainage (HAND), we found that the additional losses identified by SST are not randomly distributed across the basin. Many of these losses occur at intermediate HAND elevations (10-20 m), where buildings sit near their flooding threshold and are therefore most sensitive to storm representation.

Code and data availability

The codes and data used in this study will be publically available towards the end of the manuscript review process.

Author contributions

Mohamed ElSaadani: Conceptualization, Data curation, Formal analysis, Investigation, Methodology, Software, Validation, Visualization, Writing (original draft preparation), Writing (review and editing). Emad Habib: Conceptualization, Funding acquisition, Methodology, Project administration, Supervision, Writing (original draft preparation), Writing (review and editing). Mohamed M. Morsy: Conceptualization, Methodology, Software, Validation, Visualization, Supervision, Writing (original draft preparation), Writing (review and editing).

https://doi.org/10.5194/egusphere-2026-1388
Preprint. Discussion started: 27 March 2026

Competing interests

The contact author has declared that none of the authors has any competing interests.

Financial support

This material is based upon work supported by the National Science Foundation (NSF) under Cooperative Agreement No. OIA-2418434.

Acknowledgements

The authors thank the reviewers for their helpful feedback. During the preparation of this work the author(s) used Perplexity AI in order to improve the quality of writing.

References

Amorim, R., Villarini, G., Kim, H., Jane, R. A., and Wahl, T.: A practitioner's approach to process-driven modeling of compound rainfall and storm surge extremes for coastal Texas, J. Hydrol. Eng., 30, 04025025, 2025, https://doi.org/10.1061/JHYEFF.HEENG-6482.

Apel, H., Merz, B., and Thieken, A. H.: Quantification of uncertainties in flood risk assessments, Int. J. River Basin Manag., 6, 149–162, 2008, https://doi.org/10.1080/15715124.2008.9635344.

Apel, H., Thieken, A. H., Merz, B., and Blöschl, G.: Flood risk assessment and associated uncertainty, Nat. Hazards Earth Syst. Sci., 4, 295–308, 2004, https://doi.org/10.5194/nhess-4-295-2004.

Awaad, M. S., Habib, E. H., and Saad, H. A.: Effect of managing tributary flows on flood risk in transitional low-gradient river systems, J. Flood Risk Manag., 18, e70094, 2025, https://doi.org/10.1111/jfr3.70094.

Bodoque, J. M., Esteban-Muñoz, Á., and Ballesteros-Cánovas, J. A.: Overlooking probabilistic mapping renders urban flood risk management inequitable, Commun. Earth Environ., 4, 279, 2023, https://doi.org/10.1038/s43247-023-00940-0.

Brunner, G. W.: HEC-RAS River Analysis System: Hydraulic User's Manual, Version 1.0, 1995.

Büchele, B., Kreibich, H., Kron, A., Thieken, A., Ihringer, J., Oberle, P., and Nestmann, F.: Flood-risk mapping: contributions towards an enhanced assessment of extreme events and associated risks, Nat. Hazards Earth Syst. Sci., 6, 485–503, 2006, https://doi.org/10.5194/nhess-6-485-2006.

Chen, Y. C.: A tutorial on kernel density estimation and recent advances, Biostat. Epidemiol., 1, 161–187, 2017, https://doi.org/10.1080/24709360.2017.1396742.

Dewitz, J.: National land cover database (NLCD) 2019 products (ver. 3.0, February 2024), U.S. Geol. Surv. Data Release, 2021.

https://doi.org/10.5194/egusphere-2026-1388
Preprint. Discussion started: 27 March 2026

Dunn, C. N.: Flood damage and damage reduction calculations using HEC's Flood Impact Analysis Model (HEC-FIA), in: Building Partnerships, 1–10, 2000, https://doi.org/10.1061/40517(2000)180.

Dutta, D., Herath, S., and Musiake, K.: A mathematical model for flood loss estimation, J. Hydrol., 277, 24–49, 2003, https://doi.org/10.1016/S0022-1694(03)00084-2.

Eldardiry, H., Habib, E., and Zhang, Y.: On the use of radar-based quantitative precipitation estimates for precipitation frequency analysis, J. Hydrol., 531, 441–453, 2015, https://doi.org/10.1016/j.jhydrol.2015.05.016.

Eldardiry, H., Habib, E., Zhang, Y., and Graschel, J.: Artifacts in Stage IV NWS real-time multisensor precipitation estimates and impacts on identification of maximum series, J. Hydrol. Eng., 22, E4015003, 2017, https://doi.org/10.1061/(ASCE)HE.1943-5584.0001291.

Feldman, A. D.: Hydrologic Modeling System HEC-HMS: Technical Reference Manual, U.S. Army Corps of Engineers, Hydrologic Engineering Center, 2000.

Grimley, L. E., Sebastian, A., Leijnse, T., Eilander, D., Ratcliff, J., and Luettich, R.: Determining the relative contributions of runoff, coastal, and compound processes to flood exposure across the Carolinas during Hurricane Florence, Water Resour. Res., 61, e2023WR036727, 2025, https://doi.org/10.1029/2023WR036727.

Gutenson, J. L., Tavakoly, A. A., Islam, M. S., Wing, O. E., Lehman, W. P., Hamilton, C. O., and Massey, T. C.: Comparison of estimated flood exposure and consequences generated by different event-based inland flood inundation maps, Nat. Hazards Earth Syst. Sci., 23, 261–277, 2023, https://doi.org/10.5194/nhess-23-261-2023.

Habib, E., ElSaadani, M., Miles, B., Miller, R., Meselhe, E., Allison, M., and Hu, K.: A stakeholder-driven approach for enhancing streamflow monitoring networks in Louisiana, USA, JAWRA J. Am. Water Resour. Assoc., 61, e70007, 2025, https://doi.org/10.1111/1752-1688.70007.

Hershfield, D. M.: Technical Paper No. 40: Rainfall frequency atlas of the United States for durations from 30 minutes to 24 hours and return periods from 1 to 100 years, U.S. Weather Bur., Washington, DC, 1–65, 1961.

Khaddor, I., Achab, M., Soumali, M. R., and Alaoui, A. H.: Rainfall-runoff calibration for semi-arid ungauged basins based on the cumulative observed hyetograph and SCS storm model: Application to the Boukhalef watershed (Tangier, northwestern Morocco), J. Mater. Environ. Sci., 8, 3795–3808, 2017.

Lee, K. T. and Ho, J. Y.: Design hyetograph for typhoon rainstorms in Taiwan, J. Hydrol. Eng., 13, 647–651, 2008, https://doi.org/10.1061/(ASCE)1084-0699(2008)13:7(647).

Liu, Y., Wright, D. B., Quintero, F., Michalek, A., Villarini, G., and Smith, J. A.: Increasing flood hazard in the Lower Mississippi River due to extreme storm clustering, Sci. Adv., 11, eadt1868, 2025, https://doi.org/10.1126/sciadv.adt1868.

Louisiana Watershed Initiative (LWI) Environmental Data and Model Catalog (EnDMC): The Water Institute of the Gulf, available at: https://lwi.endmc.org/ (last access: 12 March 2026), 2026.

McCuen, R. H., Knight, Z., and Cutter, A. G.: Evaluation of the Nash-Sutcliffe efficiency index, J. Hydrol. Eng., 11, 597–602, 2006, https://doi.org/10.1061/(ASCE)1084-0699(2006)11:6(597).

https://doi.org/10.5194/egusphere-2026-1388
Preprint. Discussion started: 27 March 2026

Merz, B., Kreibich, H., and Apel, H.: Flood risk analysis: uncertainties and validation, Österreich. Wasser Abfallwirtsch., 60, 89–94, 2008.

Merz, B., Kreibich, H., Schwarze, R., and Thieken, A.: Assessment of economic flood damage, Nat. Hazards Earth Syst. Sci., 10, 1697–1724, 2010, https://doi.org/10.5194/nhess-10-1697-2010.

Merz, R., Thieken, A. H., and Blöschl, G.: Uncertainty analysis for flood risk estimation, in: International Conference on Flood Estimation, Berne, 2002.

Mikhailova, E. A., Altememe, A. H., Bawazir, A. A., Chandler, R. D., Cope, M. P., Post, C. J., and Schlautman, M. A.: Comparing soil carbon estimates in glaciated soils at a farm scale using geospatial analysis of field and SSURGO data, Geoderma, 281, 119–126, 2016, https://doi.org/10.1016/j.geoderma.2016.06.029.

Miles, B., Saad, H., and Habib, E.: High-resolution interoperable human-friendly naming system for hydrographic features and model elements (HRI-HydroName), Water, 17, 2900, https://doi.org/10.3390/w17192900, 2025.

Milly, P. C., Betancourt, J., Falkenmark, M., Hirsch, R. M., Kundzewicz, Z. W., Lettenmaier, D. P., and Stouffer, R. J.: Stationarity is dead: Whither water management?, Science, 319, 573–574, 2008, https://doi.org/10.1126/science.1151915.

Mishra, S. K. and Singh, V. P.: Soil Conservation Service curve number (SCS-CN) methodology, 42, Springer Science & Business Media, 2013.

Moftakhari, H., Salvadori, G., AghaKouchak, A., Sanders, B. F., and Matthew, R. A.: Compounding effects of sea-level rise and fluvial flooding, Proc. Natl. Acad. Sci. USA, 114, 9785–9790, 2017, https://doi.org/10.1073/pnas.1620325114.

Nelson, B. R., Prat, O. P., Seo, D. J., and Habib, E.: Assessment and implications of NCEP Stage IV quantitative precipitation estimates for product intercomparisons, Weather Forecast., 31, 371–394, 2016, https://doi.org/10.1175/WAF-D-14-00112.1.

Nobre, A. D., Cuartas, L. A., Hodnett, M., Rennó, C. D., Rodrigues, G., Silveira, A., and Saleska, S.: Height above the nearest drainage: a hydrologically relevant new terrain model, J. Hydrol., 404, 13–29, 2011, https://doi.org/10.1016/j.jhydrol.2011.03.051.

Nofal, O. M. and Van De Lindt, J. W.: Understanding flood risk in the context of community resilience modeling for the built environment: Research needs and trends, Sustain. Resilient Infrastruct., 7, 171–187, 2022, https://doi.org/10.1080/23789689.2020.1722546.

Perica, S., Pavlovic, S., Laurent, M. S., Trypaluk, C., Unruh, D., Martin, D., and Wilhite, O.: NOAA Atlas 14: Precipitation Frequency Atlas of the United States, Volume 10: Northeastern States, 2013.

Ponce, V. M. and Yevjevich, V.: Muskingum-Cunge method with variable parameters, J. Hydraul. Div., 104, 1663–1667, 1978, https://doi.org/10.1061/JYCEAJ.0005119.

Saad, H. A. and Habib, E. H.: Assessment of riverine dredging impact on flooding in low-gradient coastal rivers using a hybrid 1D/2D hydrodynamic model, Front. Water, 3, 628829, 2021, https://doi.org/10.3389/frwa.2021.628829.

https://doi.org/10.5194/egusphere-2026-1388
Preprint. Discussion started: 27 March 2026

Saad, H. A., Habib, E. H., and Miller, R. L.: Effect of model setup complexity on flood modeling in low-gradient basins, JAWRA J. Am. Water Resour. Assoc., 57, 296–314, 2021, https://doi.org/10.1111/1752-1688.12884.

Scawthorn, C., Flores, P., Blais, N., Seligson, H., Tate, E., Chang, S., and Lawrence, M.: HAZUS-MH flood loss estimation methodology. II. Damage and loss assessment, Nat. Hazards Rev., 7, 72–81, 2006, https://doi.org/10.1061/(ASCE)1527-6988(2006)7:2(72).

Scharffenberg, W. and Harris, J.: Hydrologic Engineering Center Hydrologic Modeling System, HEC-HMS: interior flood modeling, in: World Environmental and Water Resources Congress 2008: Ahupua'A, 1–3, 2008, https://doi.org/10.1061/40976(316)632.

Schwarz, J. and Maiwald, H.: Damage and loss prediction model based on the vulnerability of building types, in: RIMAX Contributions at the 4th International Symposium on Flood Defence (ISFD4), Deutsches GeoForschungsZentrum GFZ, 2009.

Wing, O. E., Lehman, W., Bates, P. D., Sampson, C. C., Quinn, N., Smith, A. M., and Kousky, C.: Inequitable patterns of US flood risk in the Anthropocene, Nat. Clim. Change, 12, 156–162, 2022, https://doi.org/10.1038/s41558-021-01265-6.

Wright, D. B., Smith, J. A., Villarini, G., and Baeck, M. L.: Estimating the frequency of extreme rainfall using weather radar and stochastic storm transposition, J. Hydrol., 488, 150–165, 2013, https://doi.org/10.1016/j.jhydrol.2013.03.003.

Wright, D. B., Smith, J. A., and Baeck, M. L.: Flood frequency analysis using radar rainfall fields and stochastic storm transposition, Water Resour. Res., 50, 1592–1615, 2014, https://doi.org/10.1002/2013WR014224.

Wright, D. B., Bosma, C. D., and Lopez-Cantu, T.: US hydrologic design standards insufficient due to large increases in frequency of rainfall extremes, Geophys. Res. Lett., 46, 8144–8153, 2019, https://doi.org/10.1029/2019GL083235.

Wright, D. B., Derin, Y., Peng, K., and Maggioni, V.: Ensemble-based uncertainty quantification can improve satellite precipitation for hydrologic prediction, Authorea Preprints [preprint], 2025, https://doi.org/10.22541/essoar.175734611.18596494/v1.

Zhu, Z., Wright, D. B., and Yu, G.: The impact of rainfall space-time structure in flood frequency analysis, Water Resour. Res., 54, 8983–8998, 2018, https://doi.org/10.1029/2018WR023550.